

## S-COSMOS: THE *SPITZER* LEGACY SURVEY OF THE HST-ACS 2° COSMOS FIELD\*I: SURVEY STRATEGY AND FIRST ANALYSIS.

D. B. SANDERS<sup>1</sup>, M. SALVATO<sup>2</sup>, H. AUSSSEL<sup>1,3</sup>, O. ILBERT<sup>1</sup>, N. SCOVILLE<sup>2,4</sup>, J. A. SURACE<sup>5</sup>, D. T. FRAYER<sup>5</sup>, K. SHETH<sup>5</sup>, G. HELOU<sup>2,5</sup>, T. BROOKE<sup>2</sup>, B. BHATTACHARYA<sup>5</sup>, L. YAN<sup>5</sup>, J. S. KARTALTEPE<sup>1</sup>, J. E. BARNES<sup>1</sup>, A. W. BLAIN<sup>2</sup>, D. CALZETTI<sup>6</sup>, P. CAPAK<sup>2</sup>, C. CARILLI<sup>7</sup>, C. M. CAROLLO<sup>8</sup>, A. COMASTRI<sup>9</sup>, E. DADDI<sup>10</sup>, R. S. ELLIS<sup>2</sup>, M. ELVIS<sup>11</sup>, S. M. FALL<sup>6</sup>, A. FRANCESCHINI<sup>12</sup>, M. GIAVALISCO<sup>6</sup>, G. HASINGER<sup>13</sup>, C. IMPEY<sup>14</sup>, A. KOEKEMOER<sup>6</sup>, O. LE FÈVRE<sup>15</sup>, S. LILLY<sup>8</sup>, M. C. LIU<sup>1,16</sup>, H. J. MCCracken<sup>17,18</sup>, B. MOBASHER<sup>6</sup>, A. RENZINI<sup>12,19</sup>, M. RICH<sup>20</sup>, E. SCHINNERER<sup>21</sup>, P. L. SHOPBELL<sup>2</sup>, Y. TANIGUCHI<sup>22</sup>, D. J. THOMPSON<sup>23,24</sup>, C. M. URRY<sup>25</sup>, J. P. WILLIAMS<sup>1</sup>

*ApJS*: accepted 01/09/07

### ABSTRACT

The *Spitzer*-COSMOS survey (S-COSMOS) is a Legacy program (Cycles 2+3) designed to carry out a uniform deep survey of the full 2° COSMOS field in all seven *Spitzer* bands (3.6, 4.5, 5.6, 8.0, 24.0, 70.0, 160.0  $\mu\text{m}$ ). This paper describes the survey parameters, mapping strategy, data reduction procedures, achieved sensitivities to date, and the complete data set for future reference. We show that the observed infrared backgrounds in the S-COSMOS field are within 10% of the predicted background levels. The fluctuations in the background at 24  $\mu\text{m}$  have been measured and do not show any significant contribution from cirrus, as expected. In addition, we report on the number of asteroid detections in the low galactic latitude COSMOS field. We use the Cycle 2 S-COSMOS data to determine preliminary number counts, and compare our results with those from previous *Spitzer* Legacy surveys (e.g. SWIRE, GOODS). The results from this “first analysis” confirm that the S-COSMOS survey will have sufficient sensitivity with IRAC to detect  $\sim L^*$  disks and spheroids out to  $z \gtrsim 3$ , and with MIPS to detect ultraluminous starbursts and AGN out to  $z \sim 3$  at 24  $\mu\text{m}$  and out to  $z \sim 1.5 - 2$  at 70  $\mu\text{m}$  and 160  $\mu\text{m}$ .

*Subject headings*: infrared: galaxies — cosmology: observations — cosmology: large scale structure of universe — galaxies: formation — galaxies: evolution — surveys

### 1. INTRODUCTION

The Cosmic Evolution Survey (COSMOS), covering 2° is the first HST survey specifically designed to thoroughly probe the evolution of galaxies, AGN and dark matter in the context of their cosmic environment (large

\* Based on observations with the NASA/ESA *Hubble Space Telescope*, obtained at the Space Telescope Science Institute, which is operated by AURA Inc, under NASA contract NAS 5-26555; also based on data collected at : the Subaru Telescope, which is operated by the National Astronomical Observatory of Japan; the XMM-Newton, an ESA science mission with instruments and contributions directly funded by ESA Member States and NASA; the European Southern Observatory under Large Program 175.A-0839, Chile; Kitt Peak National Observatory, Cerro Tololo Inter-American Observatory, and the National Optical Astronomy Observatory, which are operated by the Association of Universities for Research in Astronomy, Inc. (AURA) under cooperative agreement with the National Science Foundation; the National Radio Astronomy Observatory which is a facility of the National Science Foundation operated under cooperative agreement by Associated Universities, Inc ; and the Canada-France-Hawaii Telescope with MegaPrime/MegaCam operated as a joint project by the CFHT Corporation, CEA/DAPNIA, the National Research Council of Canada, the Canadian Astronomy Data Centre, the Centre National de la Recherche Scientifique de France, TERAPIX and the University of Hawaii.

<sup>1</sup> Institute for Astronomy, 2680 Woodlawn Dr., University of Hawaii, Honolulu, Hawaii, 96822; sanders@ifa.hawaii.edu

<sup>2</sup> California Institute of Technology, MS 105-24, 1200 East California Boulevard, Pasadena, CA 91125

<sup>3</sup> CNRS, AIM – Unité Mixte de Recherche CEA – CNRS – Université Paris VII – UMR n° 7158, 91191 Gif-sur-Yvette, France

<sup>4</sup> Visiting Astronomer, Univ. Hawaii, 2680 Woodlawn Dr., Honolulu, HI, 96822

<sup>5</sup> Spitzer Science Center, MS 314-6, California Institute of Technology, Pasadena, CA 91125

<sup>6</sup> Space Telescope Science Institute, 3700 San Martin Drive, Baltimore, MD 21218

<sup>7</sup> National Radio Astronomy Observatory, P.O. Box 0, Socorro, NM 87801-0387

<sup>8</sup> Department of Physics, ETH Zurich, CH-8093 Zurich, Switzerland

<sup>9</sup> INAF-Osservatorio Astronomico di Bologna, via Ranzani 1, 40127 Bologna, Italy

<sup>10</sup> National Optical Astronomy Observatory, P.O. Box 26732, Tucson, AZ 85726

<sup>11</sup> Harvard-Smithsonian Center for Astrophysics, 60 Garden Street, Cambridge, MA 02138

<sup>12</sup> Dipartimento di Astronomia, Universit di Padova, vicolo dell’Osservatorio 2, I-35122 Padua, Italy

<sup>13</sup> Max Planck Institut für Extraterrestrische Physik, D-85478 Garching, Germany

<sup>14</sup> Steward Observatory, University of Arizona, 933 North Cherry Avenue, Tucson, AZ 85721

<sup>15</sup> Laboratoire d’Astrophysique de Marseille, BP 8, Traverse du Siphon, 13376 Marseille Cedex 12, France

<sup>16</sup> Alfred P. Sloan Research Fellow

<sup>17</sup> Institut d’Astrophysique de Paris, UMR7095 CNRS, Université Pierre et Marie Curie, 98 bis Boulevard Arago, 75014 Paris, France

<sup>18</sup> Observatoire de Paris, LERMA, 61 Avenue de l’Observatoire, 75014 Paris, France

<sup>19</sup> European Southern Observatory, Karl-Schwarzschild-Str. 2, D-85748 Garching, Germany

<sup>20</sup> Department of Physics and Astronomy, University of California, Los Angeles, CA 90095

<sup>21</sup> Max Planck Institut für Astronomie, Königstuhl 17, Heidelberg, D-69117, Germany

<sup>22</sup> Physics Department, Graduate School of Science, Ehime University, 2-5 Bunkyo, Matuyama, 790-8577, Japan

<sup>23</sup> Caltech Optical Observatories, MS 320-47, California Institute of Technology, Pasadena, CA 91125

<sup>24</sup> Large Binocular Telescope Observatory, University of Arizona, 933 N. Cherry Ave., Tucson, AZ 85721

<sup>25</sup> Department of Astronomy, Yale University, P.O. Box 208101, New Haven, CT 06520-8101

scale structure – LSS) in a contiguous field that samples a volume in the high redshift universe approaching that sampled locally by the Sloan Digital Sky Survey (SDSS). An overview of the COSMOS project, including a full characterization of the field and a description of the vast amount of multi-wavelength data which has been, and will be, assembled is given by Scoville et al. (2006).

The *Spitzer*-COSMOS (S-COSMOS) deep IRAC and MIPS data are critical to address two major goals of the COSMOS survey: the stellar-mass assembly of galaxies (primarily from IRAC) and a full accounting of the luminosity from dust-embedded sources such as merging starburst galaxies and AGN (MIPS and IRAC). IRAC measures the light from long-lived stars in galaxies over the redshift range  $0.5 < z < 6$  (e.g., Mobasher et al. 2005). With morphological information from the HST-ACS imaging, we will be able to determine how the mass-assembly depends on morphological type, environment and redshift, in addition to other properties such as X-ray and radio emission. IRAC data are also critical for determining accurate photometric redshifts for galaxies at  $z > 1$  (e.g., Rowan-Robinson et al. 2005), where the peak of the stellar light has been redshifted into the IRAC bands. MIPS observations allow a determination of the total star formation rate (SFR) without requiring large corrections for extinction in galaxies, and will be used to quantify the connection between the SFR and the merger/interaction rate (e.g., Kartaltepe et al. 2006; Kampczyk et al. 2006) and the dependence on clustering environment (derived from spectroscopic and photometric redshifts). Deep COSMOS radio images (Schinnerer et al. 2006) will also be used to provide a secondary calibration of SFRs. In addition, both IRAC and MIPS probe the wavelength range where obscured AGN have much of their bolometric luminosity. If the AGN are heavily-obscured they may be missing from the XMM-COSMOS survey, which is the primary basis for AGN selection (Impey et al. 2006), but they will appear in the catalogs of infrared point sources. Mid-infrared selection has been shown to be  $\sim 60\%$  more efficient in selecting highly obscured AGN (Polletta et al. 2006). The COSMOS field, with its size, deep mid-IR coverage and extensive UV/X-Ray/Radio/Optical data set offers the possibility to both significantly improve the constraint on the surface density of obscured AGN and to improve our understanding of their spectral energy distributions (SEDs).

This paper presents the infrared properties of the COSMOS field, summarizes our mapping strategy, and presents the initial quick-look results from our Cycle 2 Legacy observations, all of which were completed during the 2005 December - 2006 January, visibility window. Section 2 briefly summarizes the general properties of the COSMOS Field (e.g. location, expected infrared backgrounds), and §3 lays out the mapping strategy used to obtain coverage of the full field with both the IRAC and MIPS cameras. The methods used to reduce our Cycle 2 data are presented in §4. Section 5 presents results from our preliminary analysis of the Cycle 2 data, including measured background levels and sensitivities, preliminary number counts, and asteroid detections. Our future science goals are summarized in §6.

## 2. FIELD CHARACTERIZATION

### 2.1. Field location

The COSMOS field is equatorial to ensure coverage by all astronomical facilities (centered at J2000 RA =10:00:28.6, Dec = +02:12:21.0). Our field was chosen to be devoid of bright X-ray, UV, and radio sources. The time requirements for imaging over a total area of  $2\text{ }^\circ$  and ground-based spectra of 50,000 galaxies at  $I_{\text{AB}} < 25$  mag makes it strategically imperative that the field be readily observable now and in the future by all large optical/IR telescopes and especially all unique astronomical instruments (e.g. ALMA, EVLA, SKA, TMT, JCMT/SCUBA2).

### 2.2. IR Backgrounds

The COSMOS field was chosen to have among the lowest (and most uniform) mean IRAS-100  $\mu\text{m}$  background level for an equatorial field of its size. Figure 1 shows the field outline (red square in the left panel; see caption for details) superimposed on a map of extinction computed from the reddening map of Schlegel et al. (1998), illustrating the apparent lack of contamination from foreground Galactic Plane dust clouds, as well as the lack of any strong radio and X-Ray sources which could compromise deep radio and X-ray observations of the field. Figure 1 also shows in histogram form the distribution of 100  $\mu\text{m}$  IRAS pixels within the COSMOS field versus the larger surrounding VVDS field. The sharp peak near 0.9 MJy/sr, and the lack of the higher background tail that plagues the larger VVDS region (dashed blue box in Figure 1, left panel), illustrates the choices made in shifting the final COSMOS field center to truly minimize the far-infrared background levels.

Although lower background fields at higher declination and higher ecliptic latitude will have slightly better sensitivities for an equal amount of integration time, these fields suffer the major deficiency that they are not readily accessible by all unique facilities – most importantly the (E)VLA and future ALMA which are vital for multi-wavelength studies and the future 30m optical telescope which is likely to be unique. We believe that the accessibility to all instruments far outweighs the relatively small loss ( $\sim 35\%$ ) in sensitivity for Spitzer observations of the COSMOS field.

## 3. OBSERVING STRATEGY

Because the HST-COSMOS field is close to the ecliptic, the orientation of the detectors is always the same to within a few degrees. This allowed specification of a maximally efficient tiling strategy, since we could accurately predict the orientation of the detectors. Neither of the mapping options available in the Astronomical Observation Template (AOT) allowed us the flexibility to tile given the fact that the COSMOS ACS data is aligned along the RA-DEC coordinate axes, so instead the fields have been placed using the “cluster offset” option.

### 3.1. Cycle 2: IRAC-deep Coverage

The IRAC camera has two field of views (FOVs), each one dedicated to two channels – one for the 3.6  $\mu\text{m}$  and 5.6  $\mu\text{m}$  detectors, and one for the 4.5  $\mu\text{m}$  and 8.0  $\mu\text{m}$  detectors. The two FOVs are separated on the sky by  $7^\circ$ . In order to fully cover the ACS-COSMOS field at nominal depth with all four IRAC bands, we had to map a slightly larger region of the sky, as shown in Figure 2.

The following four constraints dictated our final choice for the map tiling: (1) The maximum size of an IRAC Astronomical Observation Request (AOR) is 6 hrs, and in practice must be less than 5 hrs.; (2) Because the HST-COSMOS field is near the ecliptic plane, asteroids were expected to be a significant contaminant. We required multiple epochs separated by 1 – 2 hrs for asteroid rejection, plus each epoch must have enough redundancy to allow for cosmic ray rejection; (3) Each epoch had to have at least 4 – 5 dithers per point on the sky for adequate redundancy when reducing the data. A total of four epochs were observed; (4) IRAC has 2 FOVs separated by  $7'$ . The orientation of the FOVs was dictated by the orientation of the spacecraft on the day of the observation. Both FOVs had to observe the entire field.

The basic parameters of the tiling are a  $4 \times 4$  grid of AORs, where each AOR is composed of a grid of  $5 \times 5$  IRAC FOVs. Each AOR in the  $4 \times 4$  grid was repeated sequentially three times, resulting in three individual epochs separated by a few hours. The east and south edges are trimmed to match the HST-COSMOS field boundary. The fields overlap by tens of arcsecs, and are highly dithered. Each epoch was further offset half an array width relative to its predecessor in order to ensure an even higher number of total dither positions in the final coaddition of all epochal data in order to minimize array-position dependent calibration effects. Figure 2 shows the final area coverage resulting from our tiling strategy for the two IRAC FOVs. The total time for the IRAC-deep full-field mapping observations (all carried out in Cycle 2) was 166 hrs (see Table 1).

### 3.2. Cycle 2: MIPS Coverage

In Cycle 2, a total of 58.2 hrs were allocated for MIPS observations of the COSMOS field. The entire field was mapped at a shallow depth to check for possible cirrus structure within the COSMOS field, and deep observations over a small  $30' \times 20'$  region were carried out to quantify the ability of Spitzer to integrate down within the COSMOS field (see solid red line in Figure 2). The data were taken in MIPS scan mode with  $148''$  cross-scan offsets between the forward and return scan legs. The shallow observations were taken at the medium scan rate with  $1.75^\circ$  scan legs. These shallow observations cover  $1.75^\circ \times 1.97^\circ$  to a depth of 80 sec, 40 sec, and 8 sec for the  $24 \mu\text{m}$ ,  $70 \mu\text{m}$ , and  $160 \mu\text{m}$  arrays, respectively.

The MIPS-deep “Test area” observations were taken at the slow scan rate with  $0.5^\circ$  scan legs. These deep observations cover  $0.5^\circ \times 0.33^\circ$  to a depth of approximately 3200 sec, 1560 sec, 320 sec for the  $24 \mu\text{m}$ ,  $70 \mu\text{m}$ , and  $160 \mu\text{m}$  arrays respectively. The small “Test area” was mapped 15 times using dithers between each map to account for the bad blocks within the  $70 \mu\text{m}$  and  $160 \mu\text{m}$  arrays and to spread out the overlapping  $24 \mu\text{m}$  coverage uniformly over the field. Both forward and reverse scan mapping were done to help characterize any long-term transients as a function of scan direction.

### 3.3. Cycle 3: MIPS-deep Coverage of the Full-Field

In Cycle 3, 396.2 hrs have been allocated for deep MIPS observations covering the full COSMOS field. These observations will be taken in two epochs (2007, January and 2007, May) to help minimize the zodiacal background

and thus to maximize the achieved sensitivity. The observations during the two epochs will of necessity have different instrumental orientations (see Figure 3). The field will be fully mapped 13 times at the slow scan rate with  $148''$  cross-step offsets between the adjacent  $1.5^\circ$  scan legs. The field will also be mapped once at the medium scan rate to confirm the consistency of the calibration between the Cycle 2 and Cycle 3 data sets for the same integration time. The Cycle 3 observations will cover  $1.5^\circ \times 1.64^\circ$  to a depth of approximately 2800 sec, 1400 sec, and 280 sec for the  $24 \mu\text{m}$ ,  $70 \mu\text{m}$ , and  $160 \mu\text{m}$  arrays respectively (see Figure 3).

## 4. DATA REDUCTION (CYCLE 2)

### 4.1. IRAC

The S-COSMOS data were initially processed by the Spitzer Science Center<sup>27</sup> (SSC). The SSC provides the basic calibrated data (BCD) product, which are raw scientific exposures that are flux calibrated and corrected for well-understood instrumental signatures. These include dark subtraction, linearization, and flat-fielding. After receipt of the BCD images, S-COSMOS further processes them using a data pipeline adapted from the SWIRE project and described by Surace et al. (2007). This pipeline fixes numerous additional instrumental effects such as muxbleed, jailbarring, muxstripe, banding, and column pull-up and pull-down. It applies a frame-by-frame background correction for fluctuating bias levels. It corrects both long and short-term image latents, and masks straylight and filter ghosts. Finally, it applies a correction for the known array-position dependent calibration gain factors.

One caveat of this processing, which is true for all IRAC observations, is that the background on  $5'$  and larger scales is fixed to a COBE-derived background model. Operated in a shutterless mode, IRAC cannot provide an absolute measure of the sky background.

Once the frame-level images are prepared, they are reprojected to a common tangent projection and coadded using the SSC MOPEX software<sup>28</sup> (Makovoz, Khan & Moshir 2005) to create the final mosaiced image. An example of the quality of the data can be seen in Figure 4 where the whole mosaic is shown (left panel). The zoomed area (right panel) better illustrates the large space density of  $3.6 \mu\text{m}$  sources, and also shows that there are no obvious artifacts in the reduced image.

This reprojection also corrects for known image distortion. Since the BCD images are aligned to 2MASS, the final mosaics are also on the 2MASS astrometric solution, and generally have an accuracy of  $\sim 0.2''$ . Typical depth of coverage is between  $12\times$  and  $22\times$  100-second images per point on the sky. This is sufficient redundancy to reject cosmic rays with very high confidence. In general, asteroids are also rejected (since they move between observation epochs), although some low-sigma residuals from slow moving objects remain. These are easily identified by their color.

### 4.2. MIPS

The MIPS  $24 \mu\text{m}$  data have been reduced using a combination of our own developed IDL routines and MOPEX

<sup>27</sup> <http://ssc.spitzer.caltech.edu/>

<sup>28</sup> <http://ssc.spitzer.caltech.edu/postbcd/>

(Makovoz, Khan & Moshir 2005). Our starting point is the BCD products generated by the SSC pipeline version S13.2, where the data is flux calibrated. Great attention has been given to the subtraction of the zodiacal background, the dominant source of diffuse emission at  $24\ \mu\text{m}$  at the ecliptic latitude of S-COSMOS. Our goal was to check for the presence of weak structured cirrus emission in the COSMOS field: therefore, we avoided using any background subtraction method that could lower or cancel the signal from the interstellar medium (ISM). Given the large size of the field, the zodiacal background to the detectors varies across the field, from  $36.8\ \text{MJy/sr}$  to  $37.8\ \text{MJy/sr}$ , primarily as a function of the ecliptic latitude, but also as a function of the ecliptic longitude and of the MIPS scan mirror position. These values are slightly higher than the ones predicted by SPOT, as seen in table 3. This excess of zodiacal background is due to the presence of dust lanes that are not included in the model that SPOT uses for its background estimation (W. T. Reach, private communication). Following Fadda et al. (2006), we first subtracted the variations due to the scan mirror by identifying the sets of images taken at the same position and then determining the amount of variation due to the mirror position. We then subtracted the ecliptic background. The variations in this background are very smooth, and therefore do not induce any kind of structure. It was possible to fit and subtract out this background using a low order polynomial that would preserve any type of finely structured cirrus-like emission from the interstellar medium (ISM). The resulting image is shown in Figure 5. No cirrus-like structure can be seen in the main or deep map. We will now quantify this statement, by analysing the power spectrum of our maps. These are computed following the prescriptions of Miville-Deschênes et al. (2002).

Gautier et al. (1992) have shown that the power spectrum of the cirrus emission of the ISM at  $100\ \mu\text{m}$  can be approximated by the equation:

$$P(k) \propto B_{100\mu\text{m}}^2 \left( \frac{k}{k_0} \right)^{-3} \quad (1)$$

where  $k$  and  $k_0$  are spatial frequencies,  $B_{100\mu\text{m}}$  is the ISM surface brightness at  $100\ \mu\text{m}$  in units of  $\text{Jy/sr}$ , and  $P(k)$  is the power spectrum in units of  $\text{Jy}^2/\text{sr}$ . Note that while the original Gautier et al. (1992) formula had a dependency of  $B_{100\mu\text{m}}^3$ , recent results show that  $B_{100\mu\text{m}}^2$  is a better representation below a surface brightnesses of  $10\ \text{MJy/sr}$  (Ingalls et al. 2004). From this behavior, Helou & Beichman (1990) have shown that the noise fluctuations due to infrared cirrus in a resolution element are:

$$\frac{N}{1\ \text{mJy}} = 0.3 \left( \frac{\lambda}{100\ \mu\text{m}} \right)^{2.5} \left( \frac{D_t}{1\ \text{m}} \right)^{-2.5} \left( \frac{\langle B_\lambda \rangle}{1\ \text{MJy/sr}} \right)^{1.5} = \sqrt{P(k)} \quad (2)$$

where  $\lambda$  is the wavelength of observations,  $D_t$  is the telescope diameter,  $\langle B_\lambda \rangle$  is the average surface brightness of interstellar dust emission at the wavelength of observations and  $\Omega$  the measurement aperture solid angle. The predicting power of this formula has been verified to be within a factor of 2 by Kiss et al. (2001) using ISOPHOT observations. In the S-COSMOS field, we have  $\langle B_{100\mu\text{m}} \rangle = 0.9\ \text{MJy/sr}$  from the Schlegel et al.

(1998) analysis of the IRAS maps. Using typical cirrus colors from Ingalls et al. (2004), we infer that the contribution of cirrus to the confusion is expected to be of  $N = 0.1\ \mu\text{Jy}$  at  $24\ \mu\text{m}$ , well below the detection limit of the deep test field. This is illustrated in Figure 6 where the power spectrum of the main and deep test area are plotted respectively in red and green. Both spectra are dominated above  $1\ \text{arcmin}^{-1}$  by the convolution with the Spitzer-MIPS point spread function that shows an exponential decreases in the power at small scales. Note also that the average ISM emission between the main and deep component is slightly different, hence resulting in a difference of overall power spectrum normalization between the two areas. The black curve in Figure 6 is the power spectrum measured on the Schlegel et al. (1998) IRAS  $100\ \mu\text{m}$ , scaled to  $24\ \mu\text{m}$  using the square of the color ratio,  $S(100\mu\text{m})/S(24\mu\text{m})$ , from Ingalls et al. (2004), as shown in equation 1. At  $100\ \mu\text{m}$ , the IRAS map, very similar to the one displayed in Figure 1, is dominated by the cirrus structure. Indeed, its power spectrum is very close to a power law with index  $-3$ . By transferring it at  $24\ \mu\text{m}$ , we obtain an approximation of the power spectrum of the cirrus component in our map. Another approximation is given by equation 2 that gives the rms fluctuations for  $k = 10.3\ \text{arcmin}^{-1}$  in the case of Spitzer-MIPS24. Assuming a power law with index  $-3$ , we obtain the cyan curve in Figure 6. Note that we did not convolve the black and cyan curves with the Spitzer-MIPS PSF. Doing this would introduce a further exponential decrease toward high  $k$  values as seen in the ones measured on the maps. Both approximation are in extremely good agreement, and we can readily see that the cirrus emission is negligible in the field expect at the largest scales. Note that the polynomial fitting we applied to subtract the zodiacal background has suppressed the largest scales of the map, that are possibly dominated by the cirrus spectrum below  $k = 0.07\ \text{arcmin}^{-1}$ . The main conclusion from this power spectrum analysis is that the cirrus emission is negligible at all scales expect the largest map in the field: its contribution is orders of magnitude below that of the sources in the field.

Uncertainty maps for both the Main and Deep observations were produced along the field mosaic. We checked the uncertainty values produced by the S13.2 pipeline at the BCD level by producing difference images of overlapping scan legs. These images were used to detect moving objects (see section 5.3). We checked the distribution of pixels in the difference images and found that the BCD product uncertainties were over-estimated by 44%. We corrected all BCD uncertainty products for this factor before producing the mosaic. Final sensitivities were derived from the uncertainty maps, assuming a point source and using the PRF produced by the SSC for MIPS  $24\ \mu\text{m}$ . The MIPS-70 and MIPS-160 data were reduced using the online SSC BCD products following the pipeline algorithms presented in Gordon et al. (2005) and the filtering techniques of Frayer et al. (2006a). We have adopted the S13 calibration factors (based on stellar SEDs) of  $702\ \text{MJy/sr}$  and  $44.7\ \text{MJy/sr}$  per MIPS-70 and MIPS-160 units, respectively, and have applied the appropriate color corrections of 1.09 and 1.04 at  $70\ \mu\text{m}$  and  $160\ \mu\text{m}$  respectively to correct for galaxy SEDs. With future optimized processing (e.g., Frayer et al. 2006b), we hope to improve upon the current S-COSMOS  $70\ \mu\text{m}$  and  $160\ \mu\text{m}$

sensitivities (Table 4).

## 5. PRELIMINARY ANALYSIS: S-COSMOS (CYCLE 2)

### 5.1. Backgrounds and Sensitivities

From our recently completed Cycle-2 observations, we validated the quality of the field for future deep infrared observations. As shown in Table 3, we found total background levels of 37 MJy/sr, 10.5 MJy/sr, and 7.5 MJy/sr in the MIPS 24  $\mu$ m, 70  $\mu$ m, and 160  $\mu$ m bands, respectively. The background is dominated by the zodiacal background at 24  $\mu$ m and 70  $\mu$ m and is remarkably smooth over the entire COSMOS field. In addition, no strong cirrus structures were observed within the field, as demonstrated by our power spectrum analysis of the 24  $\mu$ m maps. The zodiacal background level is  $\sim 1.8 - 2\times$  higher than the low background fields on the sky such as the Lockman Hole (LH), CDF-S, HDF-N, and the Groth Strip, which all have similar backgrounds (see Lonsdale et al. (2003) and Table 3).

For an equal amount of integration time, the S-COSMOS MIPS sensitivities at 24  $\mu$ m and 70  $\mu$ m are within 35% of the lowest background fields, confirming that the MIPS sensitivities scale as expected with the square root of the background. At 160  $\mu$ m the COSMOS field has a background level, which is only 15% higher than the low background fields (only 7% lower sensitivity for the same integration time). Our Cycle 2 MIPS observations of the full-field (shallow) and the deep “Test area” (see Table 4) show that we are able to integrate down as  $\sigma \propto t^{-0.5}$ . This demonstrates our ability to achieve our expected sensitivities in the MIPS-deep observations of the full field to be carried out in Cycle 3.

A complete accounting of the measured sensitivities for our Cycle 2 IRAC and MIPS observations of the COSMOS field is given in Table 4.

### 5.2. Preliminary number counts

#### 5.2.1. IRAC number counts

A photometric catalogue has been obtained using the IRAC 3.6  $\mu$ m mosaic. The source extraction has been performed using the SExtractor software (Bertin & Arnouts 1996). Poor image quality areas have been masked (e.g. field boundary, a low coverage area on the south-west corner<sup>29</sup>, areas around saturated stars). The final “effective” area (i.e. after removing the masked regions) is  $2.3 \square^\circ$ .

Preliminary IRAC galaxy number counts are shown in Figure 7. The number counts shown are the number of discrete objects detected by SExtractor in the mid-infrared per flux per area. Due to the comparably large IRAC beam, comparison with extremely deep Subaru optical images indicates a significant difficulty in cross-identification between the optical images and the infrared images, which affects between 20% and 30% of the IRAC sources. However, what is shown here are strictly infrared number counts. Overall, the counts show broad agreement with those taken from elsewhere in the literature, demonstrating that the preliminary catalog

is substantially free of significant systematics relative to pre-existing Spitzer surveys. The S-COSMOS survey is extremely deep, and photometrically reaches below the classical confusion level of 40 beams/source at 3.6  $\mu$ m and 4.5  $\mu$ m. As a result, confusion is significant at faint levels, and this ultimately limits the completeness of the counts at  $< 1 \mu$ Jy. Below this level the number counts are systematically underestimated. Because even at the total integration time of S-COSMOS source confusion is significant, deeper surveys – e.g. IRAC North Ecliptic Pole Dark Field (Surace et al. 2004), XFLS ELAIS-N1 (Fadda et al. 2004; Rodighiero et al. 2006), and QSO HS 1700+6416 (Fazio et al. 2004; Barmby et al. 2004) – do not extend to proportionally fainter levels. Thus, while S-COSMOS is  $\sim 50\times$  shallower in integration time than those deeper surveys, it reaches similar flux levels while covering an area between 40 and 200 times larger. Thus S-COSMOS is as effective as any existing Spitzer survey for studying faint galaxy populations, but at the same time minimizes cosmic variance on one degree size scales when studying those populations due to its larger area. Surveys such as SWIRE will provide more information on cosmic variance for brighter sources due both to the larger total area coverage ( $25\times$ ) as well as sampling multiple ( $6\times$ ) fields. However, the SWIRE completeness limit is more than  $10\times$  brighter than that of S-COSMOS, and therefore cannot address the faintest decade in flux.

#### 5.2.2. MIPS number counts

A preliminary catalog has been extracted from the Full-field Shallow and Deep “Test area” images. Source detection has been performed using the IDL version of the DAOPHOT (Stetson 1987) on the S/N images. This method has been found to be the most efficient in separating the high ( $\sim 25\%$ ) fraction of blended sources in the deep area where the depth reaches below 70  $\mu$ Jy. Source fluxes were measured on the images using aperture photometry, masking out neighbouring sources that could contribute significantly. They were then scaled to total fluxes, using the MIPS 24  $\mu$ m Point Response Function (PRF) provided by the SSC, and taking the masked pixels into account. This method allows us to deal with the blending in a preliminary way.

Stars were identified using both the Robin et al. (2006) catalog derived from ACS morphology, and the 2MASS PSC catalog (Skrutskie et al. 2006) for the bright end. Additionally, we checked against our XMM point source catalog in order not to include any AGN in the star-like objects. We find that stars account for roughly 5% of the MIPS 24  $\mu$ m detections at 1 mJy. This fraction rises to 50% at the bright end of the counts.

The number counts for both the S-COSMOS full-field MIPS-shallow and MIPS-deep “Test area” images are displayed in Figure 8, together with the results from the GTO surveys compiled by (Papovich et al. 2004). The counts from the deep area agree well at their bright end with the ones from the full-field at their faint end. They also agree within the Poisson error bars with the GTO counts. The effect of stellar contamination is clearly visible in the counts on the MIPS shallow area where both the counts with and without the inclusion of stars is shown.

### 5.3. Asteroids

<sup>29</sup> IRAC Coverage of the south-west corner of the COSMOS field was partially affected by the loss of 9 AORs due to satellite transmission difficulties during our Cycle 2 observations; these AORs are scheduled to be recovered in 2006, Dec.

In the context of number counts, asteroids are considered a contaminant and are masked in the final image. On the other hand, *Spitzer* is ideally suited to study the thermal emission, especially from Main Belt Asteroids (MBAs), whose peak flux is typically measured at  $15 - 20 \mu\text{m}$ . Understanding the current Size Frequency Distribution (SFD) of the MBA population provides important insight into the evolution of the solar system, including accretion and collisional history, as well as impact hazards to the Earth. Although Tedesco et al. (2005) have suggested that the MBA population is composed of a significant fraction of smaller (sub-kilometer diameter) objects, these bodies have only been observable since the launch of *Spitzer*. Their Figure 6, based on ground-based observations of  $\sim 1.9 \times 10^6$  known asteroids and extrapolation of the SFDs of several asteroid families, suggests that the number of objects increases logarithmically with decreasing diameter. The actual number of smaller objects has been difficult to empirically determine, however, as MBA's emit most of their radiation in the mid-IR, leading to observational bias towards larger, more reflective asteroids.

Figure 9 shows the observed optical and IR SED of asteroid MBA 248, viewed at heliocentric and Spitzer-centric distances of 2.63 AU and 1.62 AU, respectively. The optical and IR emission is from reflected sunlight and thermal emission, respectively. The MBA 248 SED can be considered typical of asteroid SEDs at these wavelengths. As predicted by the widely used so-called "Standard Thermal Model" (Lebofsky & Spencer 1989), these solar system bodies are expected to emit substantially more radiation in the mid-IR than at optical wavelengths, thus making ground-based detection feasible for only a subset of the MBA population.

S-COSMOS, carried out near the ecliptic plane at  $\beta \sim -9^\circ$ , has detected more than 120 asteroids per  $\square^\circ$  at  $24 \mu\text{m}$ , down to a sensitivity limit of  $0.30 \text{ mJy}$  ( $5\sigma$ ), in the Cycle 2 MIPS-deep "Test area". For comparison, the only *Spitzer* asteroid survey carried out to date, the First Look Survey Ecliptic Plane Component (FLS-EPC), has looked at number counts in the ecliptic plane (i.e.  $\beta \sim 0^\circ$ ), from  $8 \mu\text{m}$  IRAC observations down to a sensitivity limit of  $0.08 \text{ mJy}$  ( $5\sigma$ ), and these data indicate that  $125 \pm 33$  asteroids per  $\square^\circ$  are present.

Because the SFD for the MBA population is expected to change with distance from the ecliptic plane (Brooke et al. 2003), and the sensitivity limits of the two programs are different, a direct comparison between S-COSMOS and FLS-EPC asteroid number counts cannot be made. The FLS-EPC has shown that the asteroid mid-IR color,  $S(24\mu\text{m})/S(8\mu\text{m})$ , appears to be constant over a large range of diameters and albedos (Bhattacharya et al. 2004; Meadows et al. 2004), and this result can be used to reconcile the two datasets. As the FLS-EPC suggests that  $S(24\mu\text{m})/S(8\mu\text{m}) \sim 10$  down to a sensitivity limit of  $\sim 0.08 \text{ mJy}$  ( $5\sigma$ ), a relevant comparison to S-COSMOS MIPS-deep "test area" asteroids should only be made for objects with  $S(24\mu\text{m}) \geq 0.8 \text{ mJy}$ , with latitudinal dropoff modeled by a power law (Cellino et al. 1991). As part of our future work, we plan to carry out this analysis, as well as detailed photometric analysis and thermal modeling, to refine overall number counts as discussed above, as well as to refine color values

and to determine orbits. It is anticipated that the Cycle 3 MIPS-deep observations of the full COSMOS field will detect  $\sim 12 \times$  the number of asteroids compared to what were found in the Cycle 2 MIPS-deep "Test area", thus reducing the uncertainty in the preliminary number counts per  $\square^\circ$  provided here.

## 6. DATA QUALITY AND FUTURE SCIENCE GOALS

The preliminary results from our S-COSMOS Cycle 2 IRAC and MIPS observations have confirmed expectations that the COSMOS field is one of the best equatorial fields of comparable size available for carrying out deep infrared surveys. Our preliminary analysis has demonstrated that (1) the full COSMOS field is devoid of cirrus contamination, (2) we are able to achieve our predicted sensitivities with both IRAC and MIPS cameras within the allotted integration times, (3) measured background levels were very close to those predicted, demonstrating our ability to minimize the zodiacal background levels through judicious use of the visibility windows, and (4) our observing methods allow for efficient removal of asteroid "contaminants", and in fact have resulted in the discovery of many new Main Belt Asteroids.

The IRAC and MIPS sensitivities achieved in Cycle 2, (and expected for Cycle 3 MIPS), will allow us to carry out the two main science goals of S-COSMOS: a study of the stellar-mass assembly of galaxies and a full accounting of the luminosity from dust-embedded sources such as merging starburst galaxies and AGN, primarily in the redshift range  $z \sim 0.5 - 3$  where COSMOS is designed to study galaxy evolution as a function of large-scale structure environment and redshift (Scoville et al. 2006).

An estimate of the numbers of galaxies that will be detected by S-COSMOS can be made using the SEDs shown in Figure 11, along with the local LF for infrared-selected galaxies (e.g., Sanders et al. 2003) and a model for evolution of the LF with redshift (e.g., Kim & Sanders 1998; Sanders 2003). Figure 11 shows four redshifted galaxy SEDs together with the measured sensitivities for the S-COSMOS and HST-ACS surveys. Included are a massive bulge-dominated system ("M87-like"), an actively star-forming disk ("M51-like"), and both "cool" and "warm" ultra-luminous IR/merging systems (e.g. Arp 220, Mrk 231) with varying mixtures of starburst and AGN activity. Our integration time of  $\sim 1200 \text{ sec}$  per pixel in each of the four IRAC bands is sufficient to easily detect  $\sim L^*$  disks and spheroids out to  $z \sim 3$ . The total number of objects detected by IRAC over the full COSMOS is expected to be  $\gtrsim 10^6$  as determined from the differential number counts at  $3.6 \mu\text{m}$  (see Figure 7). The MIPS-deep integration times of  $\sim 3000 \text{ sec}$  at  $24 \mu\text{m}$  will allow us to detect luminous infrared galaxies (LIRGs:  $L_{\text{ir}} > 10^{11} L_\odot$ ) out to  $z \sim 2$ , and ultraluminous infrared galaxies (ULIRGs:  $L_{\text{ir}} > 10^{12} L_\odot$ ) out to  $z \sim 3$ . To compute the total number of objects expected to be detected by MIPS, we have assumed strong evolution of the form  $(1+z)^{5.5}$  for objects with  $L_{\text{ir}} \gtrsim 3 \times 10^{11} L_\odot$ , consistent with the strong evolution either measured or inferred from previous studies (e.g., Sanders 2003; Oyabu et al. 2005; Le Floc'h et al. 2005) which show that the co-moving space density of the LIRG/ULIRG population appears to increase by 2-3 orders of magnitude over the redshift range 0-2. At  $24 \mu\text{m}$  S-COSMOS should detect  $\gtrsim 10^5$  LIRGs out to  $z \sim 2$

and  $\gtrsim 3 \times 10^3$  ULIRGs out to  $z \sim 3 - 4$ . At  $70 \mu\text{m}$  and  $160 \mu\text{m}$  S-COSMOS should detect  $\sim 10^3$  ULIRGs out to  $z \sim 1.5 - 2$ .

S-COSMOS is optimal for selecting unbiased samples of AGN –almost independently of their level of obscuration. At mid-infrared wavelengths the obscuring dust that hides AGN from ultraviolet, optical, and soft X-ray surveys should be a strong and largely isotropic emitter. As shown by Lacy et al. (2004) and Stern et al. (2005) and references therein, selection based on mid-IR colors (specifically, IRAC and MIPS colors from  $3.6 \mu\text{m}$  to  $24 \mu\text{m}$ ) can not only help disentangle stars, galaxies and AGN, but can also help separate type1 and type2 AGN using the same criteria. This is crucial if one wants to quantify the fraction of type2/type1 in the universe. In fact, obscuration models that aim to resolve the hard ( $> 8 \text{ keV}$ ) X-ray background (XRB) debate whether the ratio remains constant during AGN evolution (e.g., Treister & Urry 2005), or if it varies as a function of redshift and luminosity (e.g., Gilli, Comastri & Hasinger 2006). Thus, the COSMOS field, with its size, deep mid-IR coverage, and extensive UV/X-ray/Radio/Optical data set offers not only the possibility to significantly improve the constraint on the surface density of obscured AGN, but also to improve our understanding of their spectral energy distributions (SEDs), and hence the ratio of type2/type1.

The S-COSMOS data will be combined with the full multi-wavelength COSMOS data set to compute fundamental properties of galaxies. IRAC+MIPS data will provide a much more complete accounting of the bolometric luminosity, particularly for luminous starbursts and dusty AGN. In addition, the combination of IRAC (e.g.  $5 - 8 \mu\text{m}$ ) and MIPS (e.g.  $24 \mu\text{m}$ ) data will be essential in order to provide a useful discriminant between starburst and AGN activity (e.g., Rigby et al. 2004; Prouton et al. 2004; Stern et al. 2005). The S-COSMOS IRAC and MIPS colors can also be used as an AGN versus star formation discriminator in faint radio sources (Schinnerer et al. 2006). Once a galaxy has been identified as actively forming stars, the combination of radio and Spitzer data, as well as the relatively accurate photometric, and in some cases spectroscopic redshifts, will be used to both calibrate and determine the cosmic evolution of the radio-FIR correlation for star forming galaxies. The S-COSMOS observations will also be combined with the deep radio and (sub)millimeter observations of the COSMOS field to determine accurate radio through rest-frame far-infrared SEDs of the sub-millimeter galaxies in the COSMOS field (Bertoldi et al. 2006). These observations will provide the best constraints to date on the physical conditions in the sub-millimeter galaxies, (e.g. dust temperatures, dust masses, and bolometric luminosities).

The S-COSMOS data will also be used to select different populations of new and interesting objects for further study. For example, using our IRAC S-COSMOS data in combination with our optical and near-infrared COS-

MOS data, ULIRGs can be effectively selected by the  $BzK$  criterion up to  $z \sim 2.5$  (Daddi et al. 2005), whereas a similar criterion based on the  $RJL$  bands (hence exploiting the IRAC  $3.5 \mu\text{m}$  data from S-COSMOS) will expand the selection of these objects up to  $z \sim 4$  (Daddi et al. 2004). Also, for a typical Type1 AGN SED, both our IRAC and MIPS S-COSMOS observations will detect objects with optical luminosity  $1.5 \times 10^{44}$  ergs/s, twenty times fainter than the mean luminosity of SDSS QSOs at a typical redshift of  $z = 1.5$  (Richards et al. 2006).

It is clear that S-COSMOS will provide a critical part of the overall COSMOS study of galaxy evolution at  $z \sim 0.5 - 3$ , particularly at  $z > 1$  where luminous infrared galaxies become a dominant population of extragalactic objects. Interactions and mergers are very likely responsible for driving the strong evolution seen in the LIRG/ULIRG population over the redshift range  $z \sim 0 - 2$  (e.g., Sanders 2003; Le Floch et al. 2005; Babbedge et al. 2006), and therefore galaxy environment will almost certainly play a prominent role in triggering these systems (Kauffmann et al. 2003, 2004). One of the primary goals of S-COSMOS will be to explore the role of environment in producing the LIRG/ULIRG population at  $z = 0.5 - 2.5$ , and using HST imaging, to determine the galaxy types involved in the process.

The S-COSMOS Cycle2 MIPS and IRAC reduced images and catalogs will be made publicly available in May, 2007, while the Cycle3 MIPS reduced images and catalogs will be made public in June, 2008, one year after the final S-COSMOS Cycle3 MIPS observing campaign. A more complete description of the data release products and timeline can be found on the Spitzer Legacy Program web page <<http://ssc.spitzer.caltech.edu/legacy/all.html>>

This work is based on observations made with the Spitzer Space Telescope, which is operated by the Jet Propulsion Laboratory, California Institute of Technology under NASA contract 1407. Support for this work was provided by NASA through Contract Number 1278386 issued by JPL. It is a pleasure to acknowledge the hospitality provided by the Aspen Center for Physics where the majority of this paper was written. Additional information on the S-COSMOS Legacy survey is available from the main COSMOS web site at <<http://www.astro.caltech.edu/cosmos>>. It is a pleasure to acknowledge the excellent services provided by the NASA IPAC/IRSA staff (Anastasia Laity, Anastasia Alexov, Bruce Berriman and John Good) in providing online archive and server capabilities for the COSMOS datasets. We thank Guilaine Lagache for useful comments on power spectra measurements. We would also like to thank the referee for comments and suggestions which helped clarify our presentation.

*Facilities:* HST (ACS), Spitzer (IRAC), Spitzer(MIPS).

## REFERENCES

- Babbedge, T. S. et al. 2006, MNRAS, 370, 1159  
 Barmby, P. et al. 2004, ApJS, 154, 97  
 Bhattacharya, B. et al. 2004, BAAS, 204, 4102  
 Bertin, E. & Arnouts, S. 1996, A&AS, 117, 393  
 Bertoldi, F. et al. 2006, ApJS, this volume  
 Brooke, T. et al. 2003,  
[http://ssc.spitzer.caltech.edu/documents/asteroid\\_memo.pdf](http://ssc.spitzer.caltech.edu/documents/asteroid_memo.pdf)  
 Capak, P. et al. 2006, ApJS, this volume

- Cellino, A., et al. 2001, MNRAS, 253, 561  
Chapman, S. et al. 2005, ApJ, 622, 772  
Daddi, E. et al. 2004, ApJ, 617, 747  
Daddi, E. et al. 2004, ApJ, 631, L13  
Dole, H. et al. 2004, ApJS, 154, 93  
Fadda, D. et al. 2004, AJ, 131, 128, 1  
Fadda, D. et al. 2006, AJ, 131, 2859  
Fazio, G. G. et al. 2004, ApJS, 154, 39  
Fernandez-Soto, A., Lanzetta, K. M. & Yahil, A. 1999, ApJ, 513, 34  
Franceschini, A. et al. 2001, A&A, 378, 1  
Frayser, D. T. et al. 2006a, AJ, 131, 250  
Frayser, D. T. et al. 2006b, in press (astro-ph/0606676)  
Gilli, R., Comastri, A & Hasinger, G. 2006, in The X-Ray Universe, ed. A. Wilson, (Madrid, ESA SP-604), p. 813  
Gautier, T. N. et al. 1992, AJ, 103, 1313  
Gordon, K. D. et al. 2005, PASP, 117, 503  
Grazian, A. et al. 2006, A&A, 449, 951  
Helou, G. & Beichman, C. A. 1990, in ESA, From Ground-Based to Space-Borne Sub-mm Astronomy, (SEE N91-21986 13-89), p. 117  
Holland, W. S. et al. 2003, SPIE, 4855, 1  
Impey, C. et al. 2006, ApJS, this volume  
Ingalls, J. C. et al. 2004, ApJS, 154, 281  
Kartalpepe, J. S. et al. 2006, ApJS, this volume  
Kampczyk, P. et al. 2006, ApJS, this volume  
Kauffmann, G. et al. 2003, MNRAS, 346, 1055  
Kauffmann, G. et al. 2004, MNRAS, 353, 713  
Kim, D.-C. & Sanders, D. B. 1998, ApJS, 119, 41  
Kiss, C. et al. 2001, A&A, 379, 1161  
Koekemoer, A. et al. 2006, ApJS, this volume  
Lacy, M. et al. 2004, ApJS, 154, 166  
Lebofsky, L. A. & Spencer, J. R. 1989, in Asteroids II, ed. R. Binzel, (Tucson: Univ. Arizona Press), p. 128  
Le Floch, E. et al. 2005, ApJ, 632, L169  
Lonsdale, C. J. et al. 2003, PASP, 115, 897  
Makovoz, D, Khan, I. & Moshir, M. 2005, PASP, 117, 274  
Meadows, V. S. et al. 2004, ApJS, 154, 469  
Miville-Deschênes, M.-A. et al. 2002, A&A393, 749  
Mobasher, B. et al. 2005, ApJ, 635, 832  
Oyabu, S. et al. 2005, AJ, 130, 2019  
Papovich, C., Dickinson, M. & Ferguson, H. C. 2001, ApJ, 559, 620  
Papovich, C. et al. 2004, ApJS, 154, 70  
Polletta, M. et al. 2006, ApJ, 642, 673  
Prouton, O. et al. 2004, A&A, 421, 115  
Richards, G. T. et al. 2006, AJ, 131, 2766  
Rigby, J. et al. 2004, ApJS, 154, 160  
Robin, A. et al. 2006, ApJS, this volume  
Rodighiero, G. et al. 2006, MNRAS, 371, 1891  
Rowan-Robinson, M. et al. 2005, AJ, 129, 1183  
Sanders, D. B. 2003, JKAS, 36, 149  
Sanders, D. B. et al. 2003, AJ, 126, 1607  
Schinnerer, E. et al. 2006, ApJS, this volume  
Schlegel, D. J., Finkbeiner, D. P. & Davis, M. 1998, ApJ, 500, 525  
Scoville, N. Z. et al. 2006, ApJS, this volume  
Skrutskie, M. F. et al. 2006, AJ, 131, 1163  
Stern, D. et al. 2005, ApJ, 631, 163  
Stetson, P. B. 1987, PASP, 99, 191  
Surace, J. A., & the SWIRE Team, 2004, BAAS, 36, 1450  
Surace, J. A. et al. 2007, in prep  
Taniguchi, Y. et al. 2006, ApJS, this volume  
Tedesco, E. T. et al. 2005, AJ, 129, 2869  
Treister, E. & Urry, C. M. 2005, ApJ, 630, 115



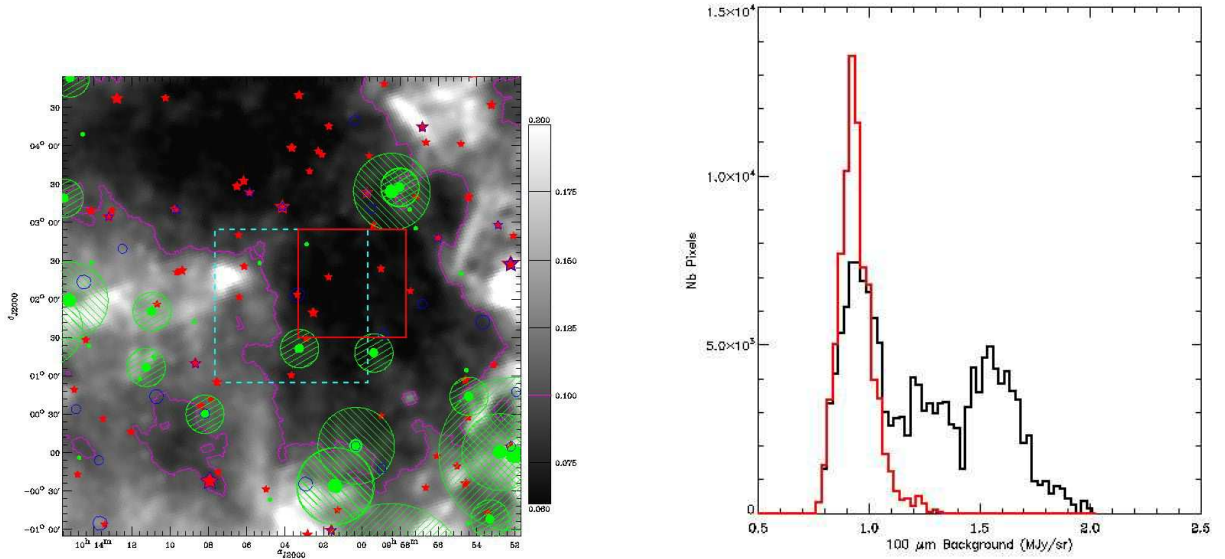


FIG. 1.— **(Left panel:)** The layout of the COSMOS Field on a map of extinction computed from the reddening map of Schlegel et al. (1998). The COSMOS Field is indicated by the red rectangle ( $1.41^\circ \times 1.41^\circ$ ) fully enclosing all of the ACS imaging, which has lower left and upper right corners (RA,DEC J2000) at  $(150.7988^\circ, 1.5676^\circ)$  and  $(149.4305^\circ, 2.8937^\circ)$ . The dashed blue box represents the  $2^\circ \times 2^\circ$  VVDS field. Tycho-2 bright stars are indicated by red stars. Bright NVSS radio sources are indicated by green dots. Radio sources with  $S_{1.4\text{GHz}} > 1\text{Jy}$ ,  $0.5\text{--}1.0\text{Jy}$ , and  $0.25\text{--}0.5\text{Jy}$ , are surrounded by an hatched area circle of radius  $1.5^\circ$ ,  $1^\circ$  and  $0.5^\circ$ , respectively. ROSAT All-Sky Survey Bright Source Catalog sources are indicated by blue circles. The purple contour represents an extinction value of  $A_V = 0.1$ . **(Right panel:)** Histogram of the distribution of  $100\ \mu\text{m}$  *IRAS* emission over the entire  $2^\circ \times 2^\circ$  COSMOS field (red) compared to the larger VVDS field (black).

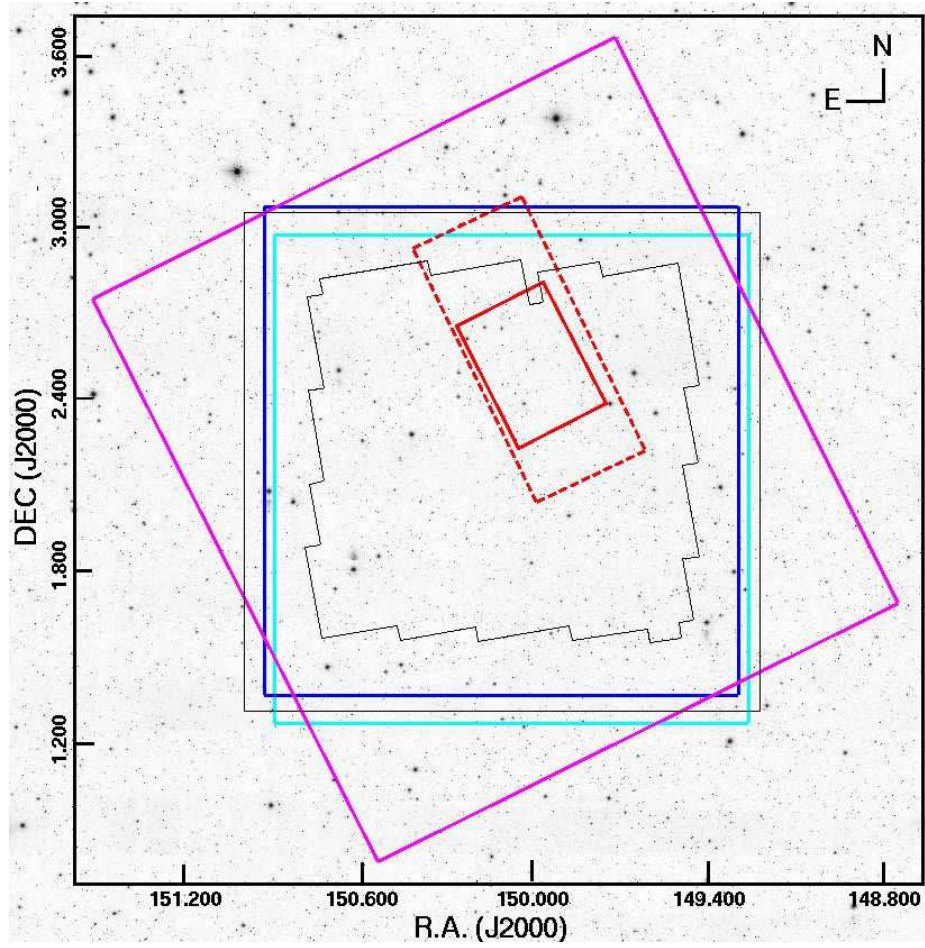


FIG. 2.— Visualization of the S-COSMOS Cycle 2 IRAC and MIPS AOR coverage. The background image is from the SDSS. Thin black square=CFHT/I-band, thick black polygon=ACS/i-band, Magenta square=MIPS-shallow, Dashed Red rectangle=MIPS-deep “Test area” coverage at  $24\ \mu\text{m}$ , Solid Red rectangle=MIPS-deep “Test area” with coverage in all three bands, Blue square=IRAC- $3.6\ \mu\text{m}$ ,  $5.4\ \mu\text{m}$ , Cyan square= IRAC- $4.5\ \mu\text{m}$ ,  $8.0\ \mu\text{m}$ . Coordinates of the corners of each box are listed in Table ??.

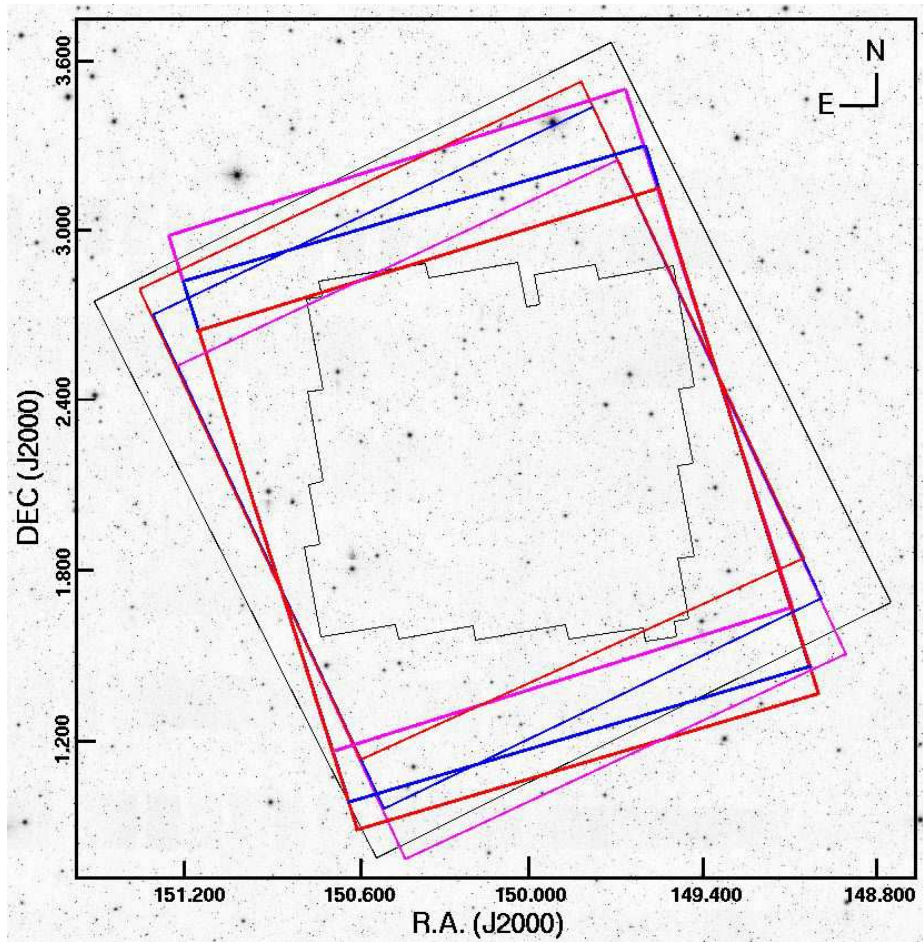


FIG. 3.— Visualization of the Cycle 3 MIPS-deep coverage of the COSMOS field. The thin black ACS and MIPS-shallow Cycle 2 observations are as in Figure 2. The blue, magenta, and red boxes are respectively, the  $24\ \mu\text{m}$ ,  $70\ \mu\text{m}$ , and  $160\ \mu\text{m}$  observations to be obtained in Cycle 3. The two “sets” of boxes represent the two different spacecraft orientations for the two epochs. Coordinates of the corners of each box are listed in Table ??.

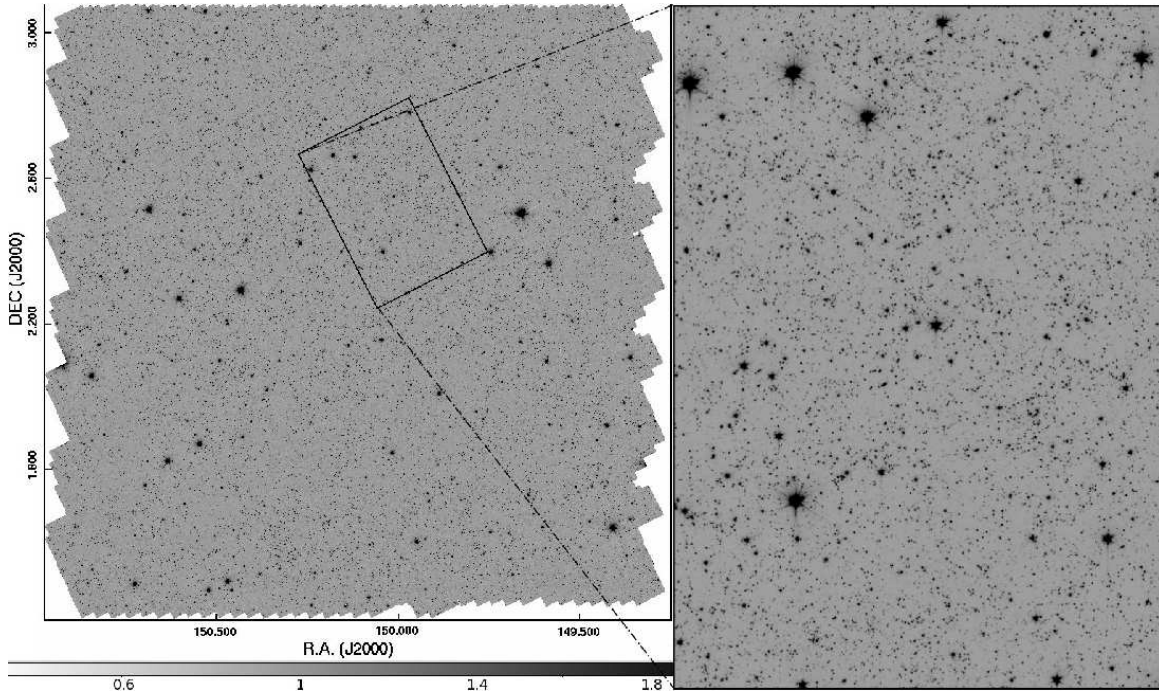


FIG. 4.— *Left panel:* Mosaic of IRAC 3.6  $\mu\text{m}$  Cycle 2 data for the whole S-COSMOS field. *Right panel:* The zoomed area corresponding to the location of the MIPS-deep “Test area” is shown for comparison with the right panel in Figure 5. The intensity scale bar is in units of  $\mu\text{Jy}$ .

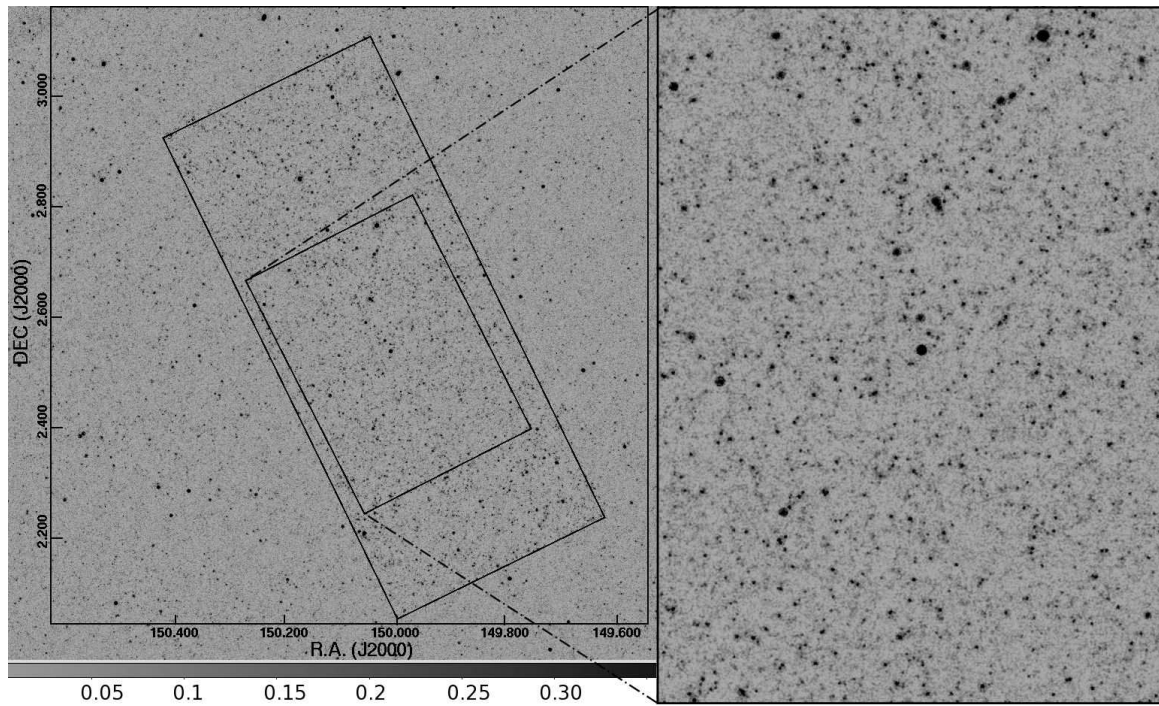


FIG. 5.— MIPS 24  $\mu\text{m}$  sources in the MIPS-deep “Test area” and larger shallow regions of the S-COSMOS field. The large rectangle insert in the left panel represents the full Cycle 2 deep coverage area at 24  $\mu\text{m}$ . The smaller rectangle and zoom in the right panel represents the Cycle 2 area with deep coverage in all three MIPS bands. The intensity scale bar is in units of mJy.

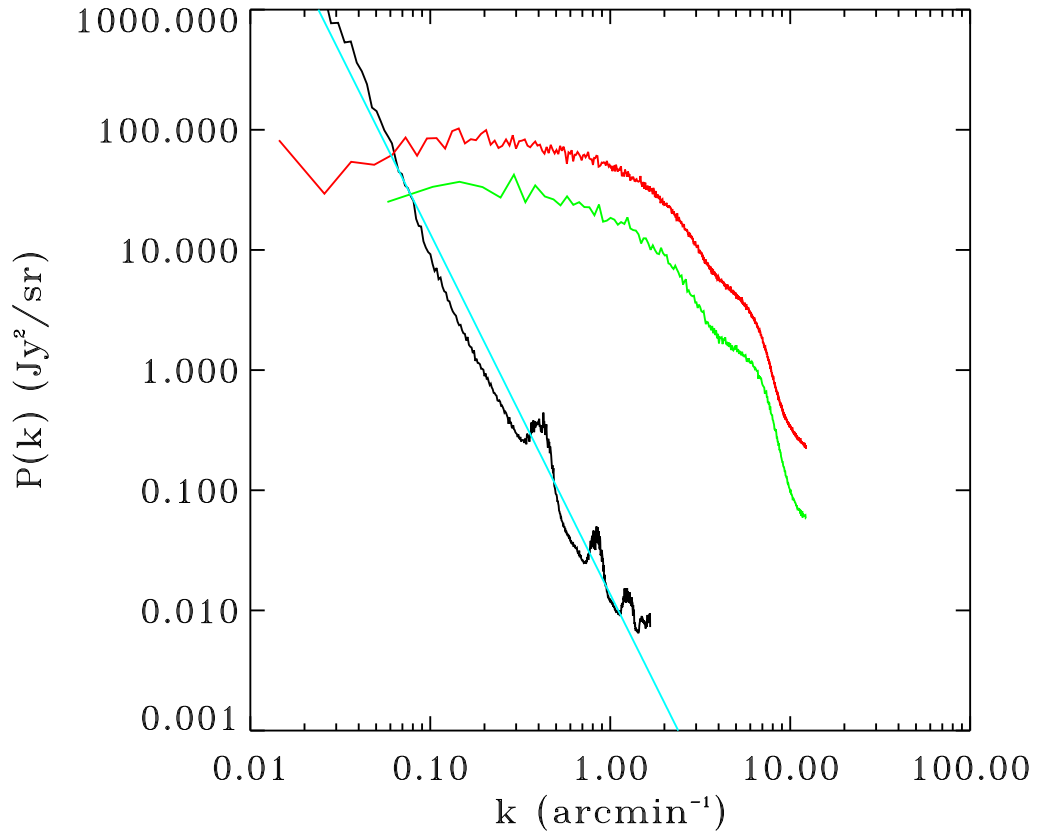


FIG. 6.— Power spectrum at  $24\ \mu\text{m}$  in the S-COSMOS area. Red: power spectrum computed on the MIPS-shallow  $24\ \mu\text{m}$  image. Green: power spectrum computed in the MIPS-deep “Test area”. Black: power spectrum computed on the IRAS  $100\ \mu\text{m}$  Schlegel et al. (1998) image (see Figure 1), and scaled to  $24\ \mu\text{m}$  using equation 1. Cyan: expected power spectrum from equation 2, assuming a power law with exponent  $-3$ . Both estimations of the cirrus contribution to the power spectrum are in good agreement, and orders of magnitude below the measured power spectrum in the maps, except at the largest scales.

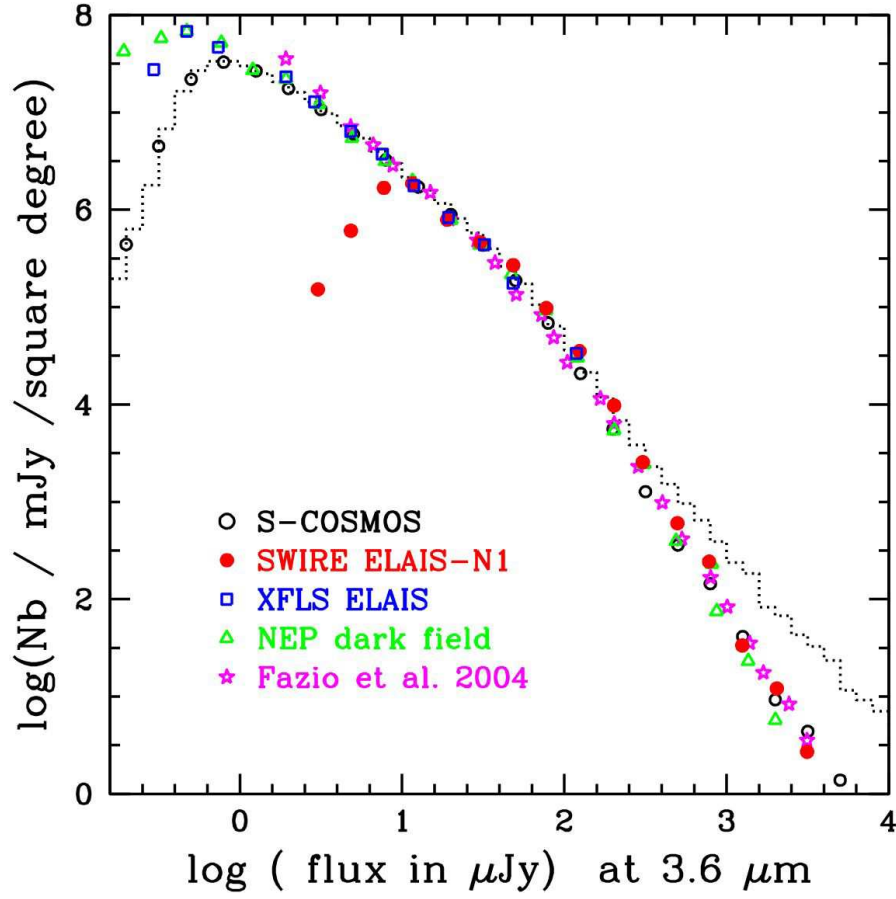


FIG. 7.— Differential number counts at  $3.6\mu\text{m}$  (IRAC-1) for the full-field Cycle 2 S-COSMOS observations. The stars are removed out to  $i'_{AB} < 23$  by using a morphological criterion, FWHM/surface brightness, as measured in the HST/ACS image (Capak et al. 2006). Given that AGN appearing as quasi stellar objects could also be removed by this criterion, we checked and found that X-ray selected AGN represent only 2% of the removed population; thus adding them back to the galaxy sample has only a small impact on the galaxy number counts. Black open circles and dotted line represent the S-COSMOS counts without and with the stars, respectively (see text). The SWIRE ELAIS-N1, XFLS ELAIS, and NEP dark field data are from Surace et al. (2007). None of the number counts have been corrected for incompleteness.

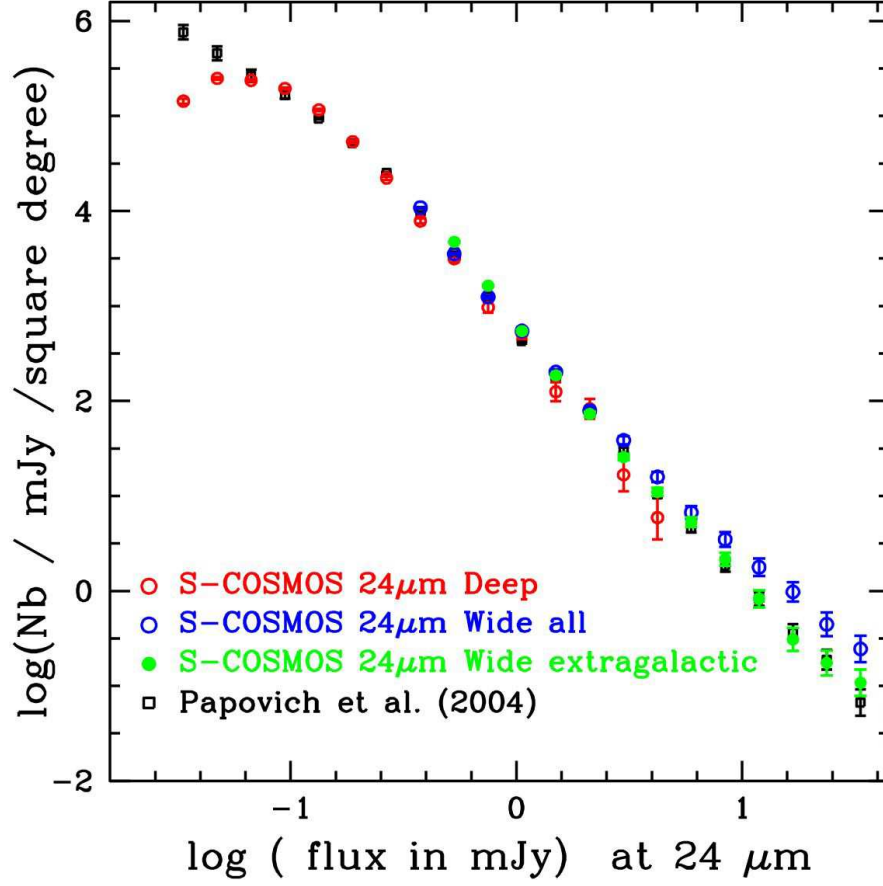


FIG. 8.— Preliminary differential counts at  $24\mu\text{m}$  from the MIPS-deep “Test area” (red) and MIPS-shallow “Wide all” (cyan) Cycle 2 S-Cosmos observations, compared to those compiled by Papovich et al. (2004). The error bars for the S-COSMOS counts are the  $1\sigma$  poissonian fluctuations. The counts in the MIPS-deep area are compatible with the Papovich counts down to our  $5\sigma$  completeness limit of  $67\mu\text{Jy}$ . In the MIPS-shallow “Wide all” observations, the excess of sources detected at large fluxes is due to stars in the field. The MIPS-shallow “Wide extragalactic” (green) counts were obtained after removal of the stars (see text).

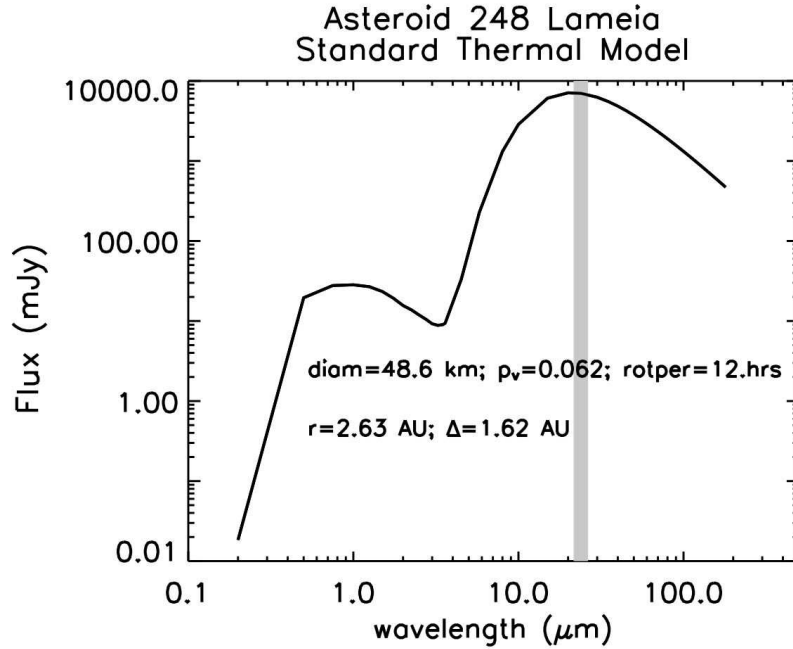


FIG. 9.— Model spectral energy distribution for main belt asteroid 248 Lameia. The Standard Thermal Model, assuming geometric albedo  $p_v = 0.062$  is used. As this object is highly non-reflective, the mid-IR emission is two orders of magnitude greater than at optical wavelengths. The grey bar represents the MIPS  $24\ \mu\text{m}$  band. This object's thermal properties are similar to those of other MBA's, making them ideally suited for detection at the S-COSMOS wavelengths of  $8\ \mu\text{m}$  and  $24\ \mu\text{m}$ .

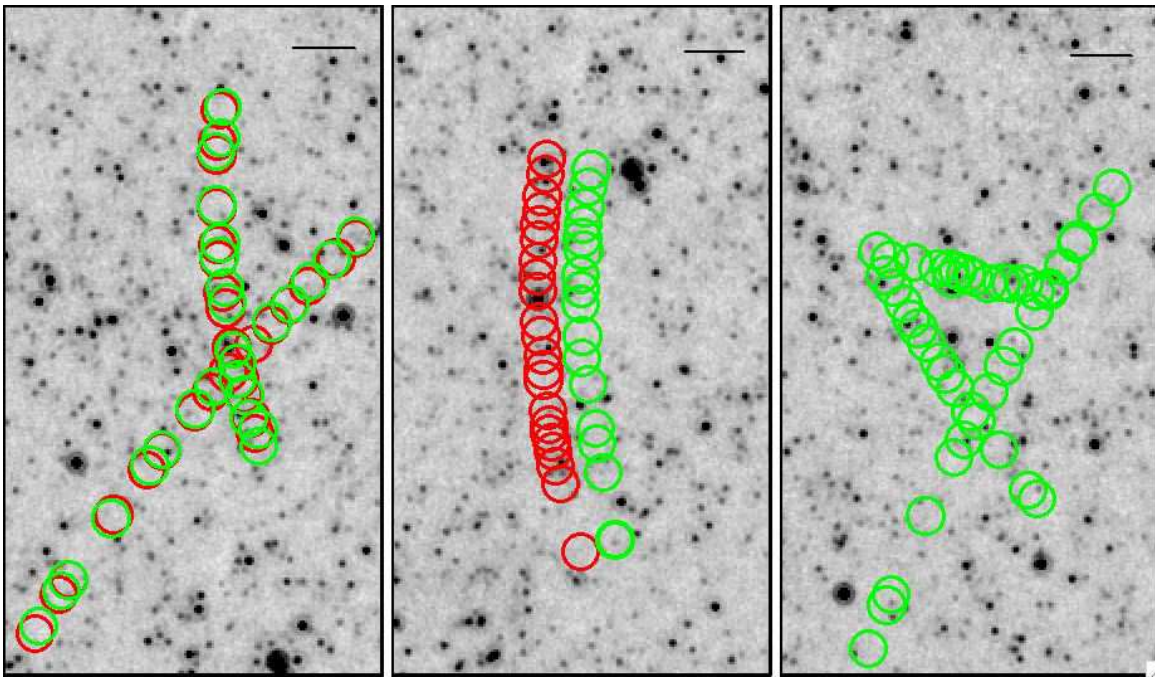


FIG. 10.— Example of asteroids and their trajectories (green circles) on the deep MIPS  $24\ \mu\text{m}$  image. The figure has the asteroids removed. Green circles reflect the original position of the removed asteroids. We queried the JPL Horizons On-Line Ephemeris Service using a Spitzer-centric line of sight (<http://ssd.jpl.nasa.gov/x/ispv.html>) in order to quantify the number of asteroids already known. Red circles reflect expected locations for the asteroids based on these queries. Less than 20% are known to the system (red circles in the first and middle panel) while 80% are new detections (right panel). Among the asteroids already known, some have a trajectory that is only approximately known, therefore an offset is measured when compared with our detections (middle panel). The scale bar in the upper right of each panel represents  $1'$ .



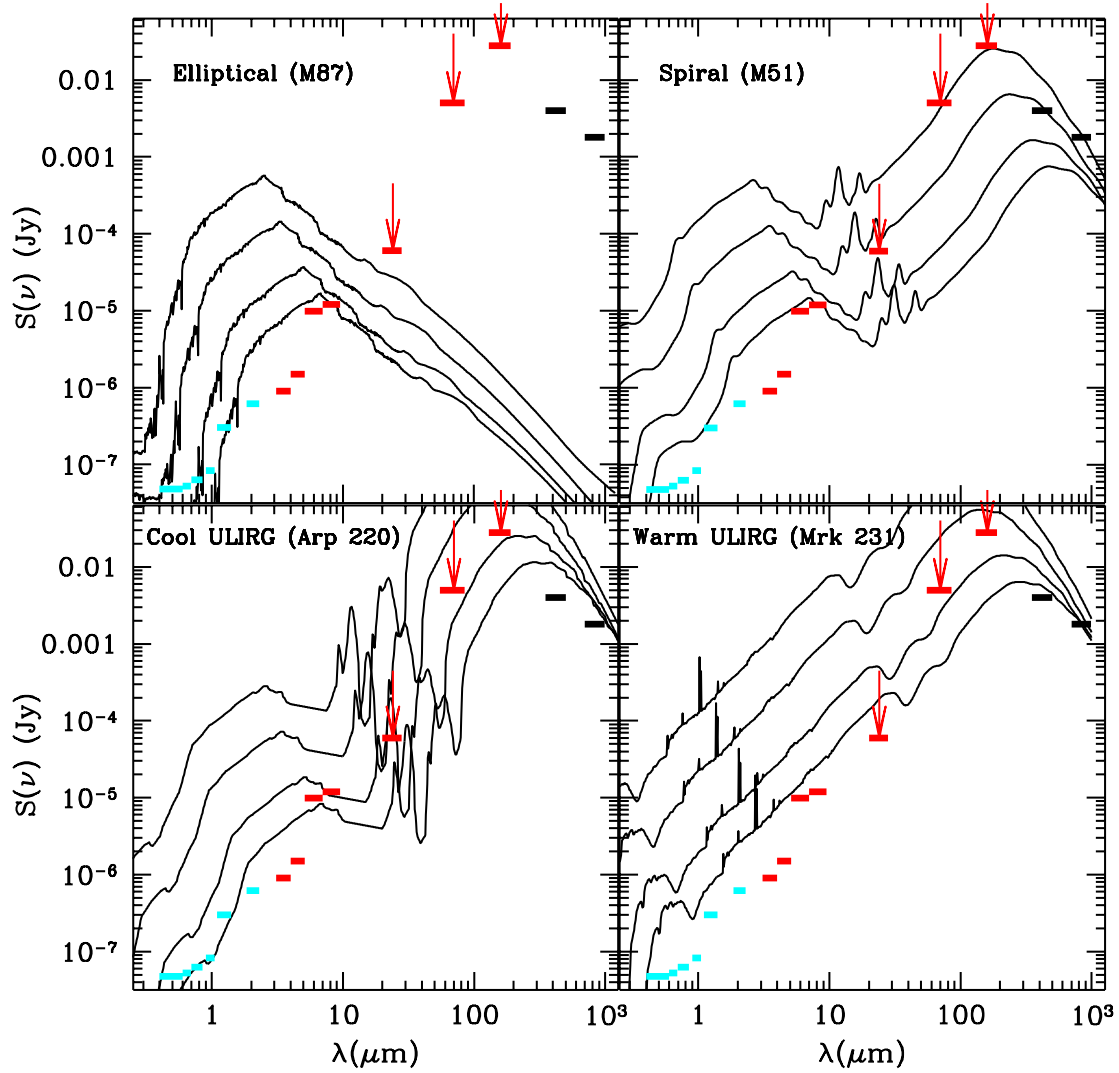


FIG. 11.— SEDs of galaxies (Franceschini et al. 2001), as a function of  $z$  ( $= 0.5, 1, 2, 3$ ) (solid curves, top-to-bottom). The Elliptical (“M87-like”) and Spiral (“M51-like”) templates have been scaled to  $L_{\text{bol}} = 10^{11} L_{\odot}$  and  $L_{\text{bol}} = 3 \times 10^{11} L_{\odot}$  respectively. The “cool” and “warm” ULIRG templates have been scaled to  $L_{\text{bol}} = 2 \times 10^{12} L_{\odot}$ . Superimposed in color are S-COSMOS and COSMOS survey sensitivities ( $5\sigma$ ): (red arrows and bars) S-COSMOS Cycle 2 MIPS-shallow and Cycle 2 MIPS-deep surveys, respectively (this paper); (magenta bars) S-COSMOS Cycle 2 IRAC survey (this paper); (blue bars) COSMOS ground-based, optical/NIR (BVR*'*i/z/JK) data (Capak et al. 2006; Taniguchi et al. 2006). The purple bars at  $450 \mu\text{m}$  and  $850 \mu\text{m}$  show the expected sensitivities ( $5\sigma$ ) from our recently approved UH+Tri-national Legacy survey of the COSMOS field with JCMT-SCUBA2 (Holland et al. 2003).

TABLE 1  
S-COSMOS (CYCLE 2) OBSERVATIONS SUMMARY TABLE

---



---

<b>IRAC-deep Scan Map Summary</b>
Three epochs, separated by 4 – 5 hrs each (1-15 Jan, 2006)
Twelve pointings of 100 sec each
Total depth = 1200 sec
Total time = 166 hrs
<b>MIPS-shallow Scan Map Summary</b>
One epoch (Jan, 2006)
Total Depth: 80 sec (24 $\mu\text{m}$ ), 40 sec (70 $\mu\text{m}$ ), 8 sec (160 $\mu\text{m}$ )
Total time = 16.6 hrs
<b>MIPS-deep “Test area” Scan Map Summary</b>
One epoch (Jan, 2006)
Total Depth: 3200 sec (24 $\mu\text{m}$ ), 1560 sec (70 $\mu\text{m}$ ), 320 sec (160 $\mu\text{m}$ )
Total time = 41.6 hrs

---

TABLE 2  
 COORDINATES FOR S-COSMOS OBSERVATIONS IN CYCLE 2 AND CYCLE 3 <sup>a</sup>

Field	Bottom Left	Top Left	Top Right	Bottom Right
IRAC 3.6/5.8	10:03:45 1:23:14	10:03:45 3:04:43	09:57:10 3:04:43	09:57:11 1:23:14
IRAC 4.5/8.0	10:03:36 1:17:38	10:03:36 2:58:53	09:57:03 2:58:53	09:57:03 1:17:38
MIPS-deep	10:00:14 2:14:35	10:01:04 2:40:11	09:59:53 2:49:29	09:59:02 2:23:13
MIPS-shallow	10:02:10 0:48:57	10:06:07 2:45:33	09:58:53 3:39:43	09:54:59 1:42:34
MIPS 24 (1)	10:02:34 1:00:37	10:04:54 2:49:46	09:58:24 3:18:15	09:55:57 1:43:03
MIPS 24 (2)	10:02:04 0:59:13	10:05:20 2:42:46	09:59:08 3:26:25	09:56:06 1:29:17
MIPS 70 (1)	10:02:47 1:11:06	10:05:05 2:59:06	09:58:41 3:30:09	09:56:21 1:41:25
MIPS 70 (2)	10:01:45 0:48:43	10:04:58 2:31:48	09:58:47 3:15:13	09:55:35 1:31:37
MIPS 160 (1)	10:02:26 0:54:47	10:04:40 2:39:16	09:58:13 3:09:09	09:55:59 1:23:13
MIPS 160 (2)	10:02:23 1:09:14	10:05:29 2:48:08	09:59:18 3:31:47	09:56:12 1:51:41

<sup>a</sup> Cycle 2 coordinates are given in rows 1–4. Cycle 3 coordinates are given in rows 5–10, where (1) and (2) refer to the different spacecraft orientations in Jan, and May, 2006, respectively. The layout of the Cycle 2 and Cycle 3 maps can be seen in Figure 2 and Figure 3, respectively

TABLE 3  
FIELD COMPARISON OF IR BACKGROUNDS, AND SENSITIVITIES WITH PREDICTED AND MEASURED S-COSMOS CYCLE-2 IRAC-DEEP AND MIPS-DEEP OBSERVATIONS.

Field	8.0 $\mu\text{m}$ (spot)		24 $\mu\text{m}$ (spot)		100 $\mu\text{m}$ ( <i>IRAS</i> )
	Bkg (MJy/sr)	S(1200 sec) ( $\mu\text{Jy}$ )	Bkg (MJy/sr)	S(3200 sec) (mJy)	Bkg (MJy/sr)
COSMOS <sup>a</sup>	6.7	14.6	31	0.065	0.90
LH, CDF-S <sup>a</sup>	5.2	12.7	19	0.053	0.45
SWIRE-XMM <sup>a</sup>	7.1	14.8	31	0.065	1.25
COSMOS <sup>b</sup>	6.9	14.6	37	0.071	0.90

<sup>a</sup> Total backgrounds predicted by SPOT at 8  $\mu\text{m}$  and 24  $\mu\text{m}$  are given for the different fields in the first three rows. Sensitivities ( $5\sigma$ ) were computed assuming 1200 sec of integration with IRAC and 3200 sec with MIPS, equivalent to our Cycle 2 integration times for IRAC and MIPS-deep, respectively. All *IRAS* 100  $\mu\text{m}$  values are actual measurements from the *IRAS* maps.

<sup>b</sup> Measured median background levels over the full  $2\Box^\circ$  COSMOS field in our S-COSMOS Cycle-2 data.

TABLE 4  
S-COSMOS (CYCLE 2) INTEGRATION TIMES AND  
MEASURED SENSITIVITIES

Camera	Band $\mu\text{m}$	Coverage (% field)	Int. time <sup>a</sup> (sec)	$5\sigma$ (mJy)
IRAC	3.6	100	1200	0.0009
IRAC	4.5	100	1200	0.0017
IRAC	5.6	100	1200	0.0113
IRAC	8.0	100	1200	0.0146
MIPS-shallow	24	100	80	0.42
MIPS-shallow	70	100	40	34.0
MIPS-shallow	160	100	8	150.0
MIPS-deep	24	8	3200	0.071
MIPS-deep	70	8	1560	7.5
MIPS-deep	160	8	320	70.0

<sup>a</sup> Median effective integration time per pixel.